Supplementary Information (SI) for Nanoscale.
This journal is © The Royal Society of Chemistry 2026

Supplementary information

Growth of Curved Single-Crystal Silicon Nanostructures via Laser-Induced Localized Thermal Gradient Steering

Xingjie Yang,[ab] Ping Chen,[ab] Shenyong Yang*[ab] and Zhikun Liu*[ab]

[a] State Key Laboratory of Micro-nano Engineering Science, School of Mechanical Engineering, Shanghai Jiao Tong University, Shanghai, 200240, P.R. China.
[b] Micro-nano Engineering Sciences Research Center, School of Mechanical Engineering, Shanghai Jiao Tong University, Shanghai, 200240, P. R. China.

Table of contents

1. Discussion of the natural oxide layer on the substrate surface 3

2. Numerical Simulation..4

3. Nucleation and growth behavior of silicon under laser irradiation within the optimized epitaxial growth window 6

4. Top-down SEM image of single vertical silicon pillar..7

5. The effect of different single-pulse energies on silicon pillars 8

6. SEM image of branched silicon structures...8

7. The effect of different laser frequencies on silicon pillars 9

8. Growth mechanism and crystallographic analysis of discontinuous tilted short pillars under non-steady-state conditions..10

9. Horizontal silicon wires of different sizes...12

10. Formation Mechanisms and Parameter-Dependent Modulation of Elliptical Cross-sections in Silicon Pillars 19

11. Elemental quantification of phosphorus-doped silicon nanowires. 23

12. SEM images of heavily doped silicon nanowires and electrodes..................................24

13. Cross-sectional area of phosphorus-doped silicon nanowires and its effect on electrical properties 25

1. Discussion of the natural oxide layer on the substrate surface

In this work, the Si substrates were cleaned via sequential sonication in acetone, isopropanol, and ultrapure water. Notably, no deoxidation pre-treatments, such as hydrofluoric acid (HF) etching, were performed, thereby retaining the native oxide layer on the substrate surface. This interfacial oxide layer typically acts as a thermodynamic and kinetic barrier to homoepitaxy.

Our observations confirmed that growth was indeed suppressed at lower laser pulse energies.[1] However, upon exceeding the energy threshold required to initiate growth, TEM and EDX mapping (Fig. S1C) revealed a critical phenomenon: while a continuous oxide layer persisted on the non-irradiated substrate regions and the exterior pillar surfaces, no oxygen signal was detected at the foundational pillar-substrate interface.

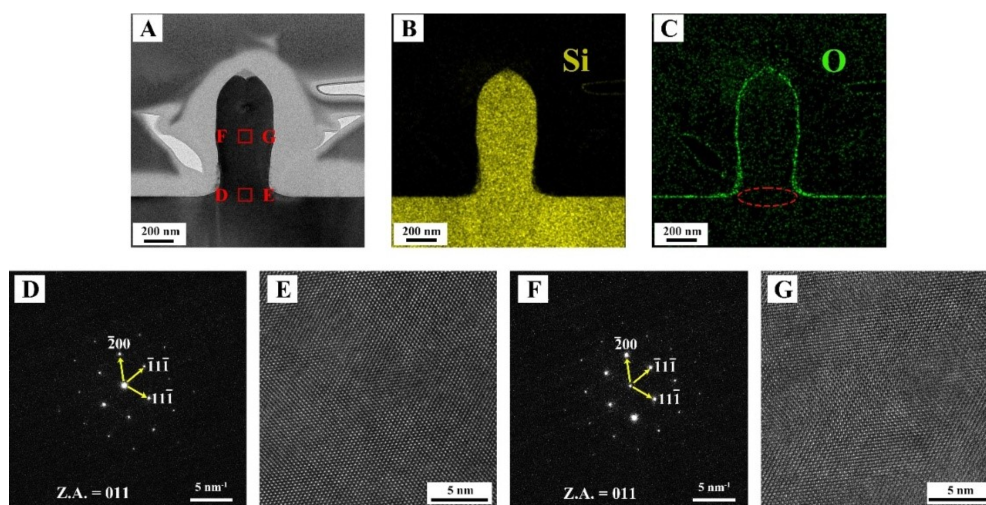

Fig. S1 TEM images of a silicon structure grown on a Si(100) substrate after FIB sectioning, using laser irradiation with a spot diameter of 2.2 μm, a frequency of 500 Hz, and a single-pulse energy of 6 nJ for 1.2 s. (A) Bright-field TEM image of the entire silicon structure after slicing. (B, C) Elemental maps showing the distributions of Si and O in (A). (D, F) are SAED patterns from the corresponding boxed regions in (A). (E, G) are high-resolution TEM images of the boxed areas in (A), acquired along the [011] zone axis.[1]

These findings suggest the existence of an in-situ oxide removal mechanism. As reported by Joyce et al.,[2] reactive silicon species are capable of reducing and decomposing surface silicon oxide at sufficiently high temperatures. Consequently, we infer that in the present study, the in-situ removal of the native oxide layer is driven by the reaction between the oxide and the reactive silicon species generated from the thermal decomposition of CHS. This process enables the selective removal of the silicon oxide layer at the growth interface, thereby facilitating homoepitaxial growth.

2. Numerical Simulation

2.1 FDTD simulation of electric field intensity distribution

To elucidate the light-matter interaction at the growth interface, the electric field intensity distribution ($|E/E_0|$) was simulated using the finite-difference time-domain (FDTD) method (Ansys Lumerical). These simulations employed a substrate featuring a representative silicon hemisphere with a radius of 150 nm. This specific radius was selected because it closely approximates the average diameter of the experimental silicon pillars and because the initial growth at the base of these structures remains predominantly vertical even under continuous scanning conditions. Consequently, the hemispherical model serves as a reasonable and accurate approximation of the physical growth interface. Based on a vertical growth rate of approximately 500 nm/s（Figure 1A）and a laser scanning speed of 200 nm/s, the time required to grow a hemisphere to a height of 150 nm is estimated at 0.3 seconds. During this interval, the accumulated lateral movement induces a 60 nm offset between the center of the silicon sphere and the center of the laser spot, which establishes the primary parameters for the numerical model.

The computational domain was structured using a cylindrical silicon substrate with a radius of 5 μm and a thickness of 2 μm. Within this domain, a hemispherical silicon protrusion with a radius of 150 nm was positioned either at the substrate center or at x = -60 nm to simulate the steady-state and scanning-induced nanostructure environments respectively. Above these features, a 1 μm-thick layer of CHS (n = 1.691,[3]) served as the dielectric medium. The optical constants for silicon were obtained from the Palik database,[4] and the laser was modeled as a Gaussian beam with a wavelength of λ = 532 nm and a focal spot diameter ($1/e^2$) of 1.4 μm, matching the experimental configuration. To ensure high numerical accuracy, a fine mesh step of 1 nm was applied. Perfectly matched layer (PML) boundary conditions were employed to eliminate non-physical reflections at the domain boundaries.

2.2 Photothermal simulation via finite element method (COMSOL)

To investigate the thermal dynamics during the growth process, a three-dimensional transient heat transfer study was conducted using COMSOL Multiphysics. Given that the electron-phonon equilibration time 10^{-12} s is significantly shorter than the laser pulse duration (6 ns), photo-excited electronic effects were neglected, and lattice heating was considered the dominant mechanism.[5-7] The electromagnetic power loss density (Q), serving as the volumetric heat source, was determined by the classical expression:[8, 9]

$$Q = \frac{1}{2}\omega\varepsilon^{''}|E|^2$$

where ω is the angular frequency of the incident light, ε'' is the imaginary part of the complex permittivity, and $|E|$ is the local electric field amplitude. The field distribution was mapped directly from FDTD simulation results ($|E/E_0|$).

The geometric model was kept consistent with the FDTD simulations, with physical parameters detailed in Table S1. Since both silicon and CHS remain in their respective condensed phases without transitioning under the optimized growth conditions, latent heat effects were excluded. Initial and boundary temperatures were set to 293.15 K. Laser pulsing was temporally modulated using the Event Interface to simulate the 6 ns pulse duration and repetition rate. To ensure numerical convergence and capture high thermal gradients, local mesh refinement was applied to the silicon hemisphere, with the element size progressively increasing toward the domain boundaries. The

simulation utilized an initial maximum time step of 0.01 ns to accurately resolve the rapid thermal fluctuations induced by the nanosecond pulses.

Table S1: Physical Parameters used in the COMSOL Photothermal Simulations

Parameters	Symbol	Value/function
Pulse duration	τ	6 ns
Beam radius	r	0.7 μm
Laser wavelength	λ	532 nm
Speed of light	C_L	3×10^8 m/s
Laser frequency	f	$C_L/\lambda=5.64\times10^{14}$ 1/s
Angular frequency	ω	$2\pi f=3.54\times10^{15}$ rad/s^2
Imaginary part of the relative permittivity	ε_r''	Reference[10]
Vacuum permittivity	ε_0	8.85×10^{-12} F/m
Imaginary part of the permittivity	ε''	$\varepsilon_0\varepsilon_r''$
Peak power	P_p	0.68 W
Peak light intensity	I_p	$\frac{2P_p}{\pi r^2}=$ 8.96×10^{11} W/m^2
Peak electric field strength	E_0	$\sqrt{\frac{2I_p}{1.691C_L\varepsilon_0}}=$ 2.00×10^7 V/m

3. Nucleation and growth behavior of silicon under laser irradiation within the optimized epitaxial growth window

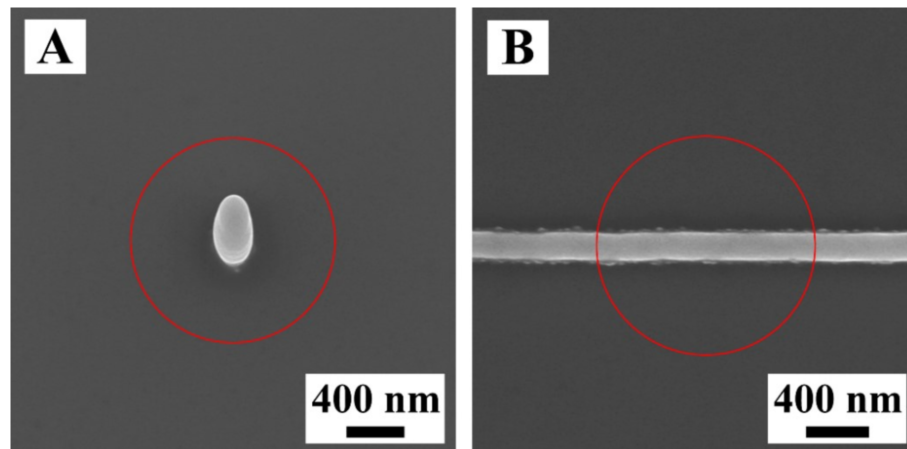

Fig. S2 Low-magnification SEM images of as-grown vertical silicon pillars and horizontal silicon lines. The red circles indicate the extent of the laser spot, demonstrating that laser irradiation does not induce uncontrolled secondary nucleation or growth on the substrate surrounding the intended structures.

4. Top-down SEM image of single vertical silicon pillar

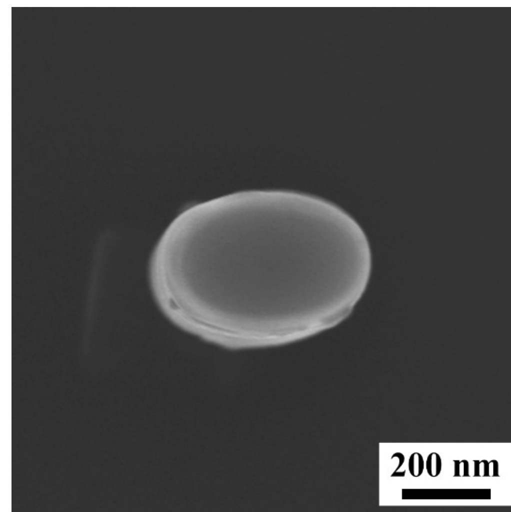

Fig. S3 Top-down SEM characterization of vertical silicon pillar illustrating growth anisotropy. The SEM image (vertical perspective) displays silicon pillar grown via stationary laser irradiation for 10 s at a single-pulse energy of 4.1 nJ and a repetition rate of 400 Hz.

5. The effect of different single-pulse energies on silicon pillars

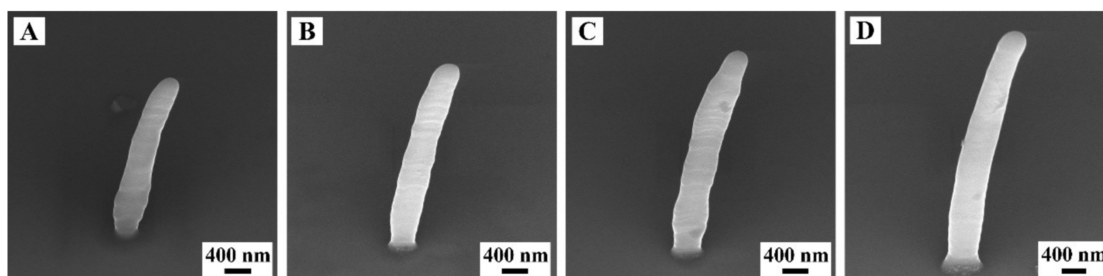

Fig. S4 Morphological dependence of silicon pillars on single-pulse laser energy. SEM images (acquired at a 45° stage tilt) illustrate the structural evolution of silicon pillars grown at a constant repetition rate of 400 Hz, a scanning velocity of 100 nm/s and growth time of 10 s. The pulse energy increases from (A) 3.9 nJ to (B) 4.4 nJ, (C) 4.6 nJ, and (D) 5.1 nJ.

As illustrated in Fig. S3 and S17, the horizontal cross-sections of the grown silicon pillars exhibit an elliptical geometry, elongated along the direction of laser polarization. During the fabrication of curved silicon pillars, the laser scanning was performed parallel to the polarization direction. The images were captured from a perspective perpendicular to the polarization; thus, the major axis of the ellipse is observed. This dimension increases with laser energy, with measured values of 430 nm (A), 485 nm (B), 515 nm (C), and 575 nm (D), respectively. A detailed discussion of the underlying influence mechanisms is provided in Section 10 of the Supporting Information.

6. SEM image of branched silicon structures

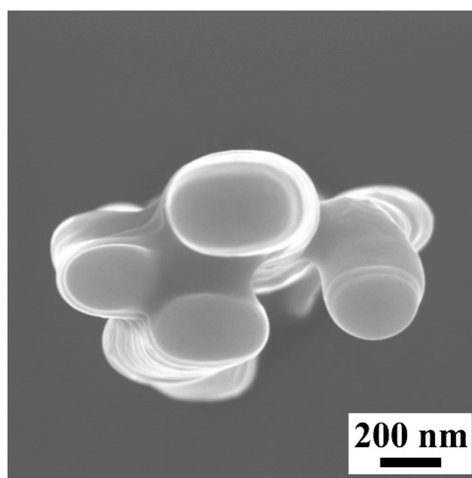

Fig. S5 Top-down SEM image of silicon structures grown under high-energy stationary irradiation. The image (vertical perspective) shows the silicon morphology resulting from 7 s of continuous irradiation at a single-pulse energy of 6.6 nJ and a repetition rate of 400 Hz.

7. The effect of different laser frequencies on silicon pillars

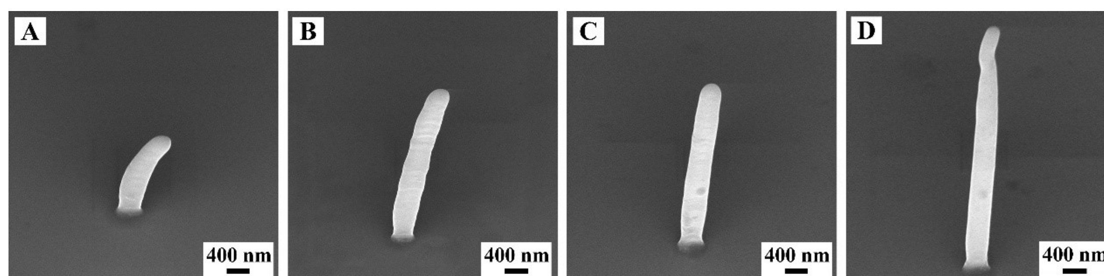

Fig. S6 Morphological dependence of silicon pillars on laser frequency. SEM images (acquired at a 45° stage tilt) illustrate the structural transition of silicon pillars grown at a constant single-pulse energy of 4.4 nJ and a scanning velocity of 100 nm/s. The global tilt angle decreases and the radius of curvature expands as the repetition rate increases from (A) 200 Hz (growth time: 10 s) to (B) 400 Hz (10 s), (C) 1000 Hz (5 s), and (D) 2000 Hz (3 s).

As illustrated in Fig. S3 and S17, the horizontal cross-sections of the grown silicon pillars exhibit an elliptical geometry that is elongated along the direction of laser polarization. During the fabrication of curved silicon pillars, the laser scanning was performed parallel to the polarization direction. Since the imaging perspective in the figure is perpendicular to the polarization, the observed dimension corresponds to the major axis of the ellipse. This major axis length decreases as the laser frequency increases, with measured values of 470 nm (A), 450 nm (B), 430 nm (C), and 415 nm (D), respectively. A comprehensive discussion regarding the underlying influence mechanisms is provided in Section 10 of the Supporting Information.

8. Growth mechanism and crystallographic analysis of discontinuous tilted short pillars under non-steady-state conditions

Experimental observations reveal that when the vertical growth of the silicon is interrupted by excessively high scanning speeds (e.g., ≥ 200 nm/s), leading to the formation of uncontrollable and discontinuous tilted silicon pillars, the morphology of the nanostructure tip undergoes an evolution from a smooth, dome-like profile into a distinct "tip" feature. This feature is frequently accompanied by randomly distributed small particles at the apex (Fig. S7).

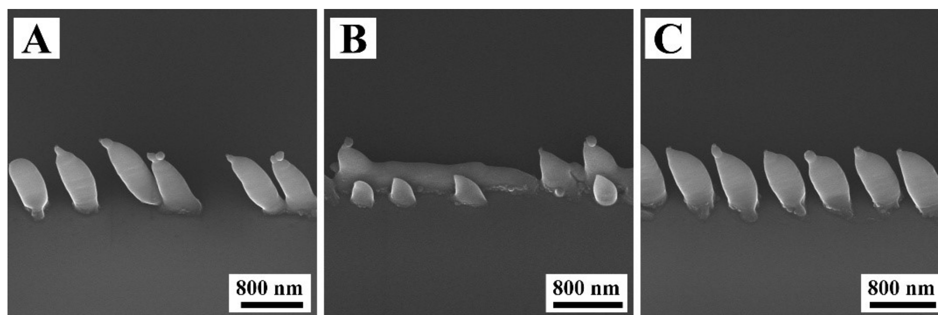

Fig. S7 SEM images of tilted short silicon pillars grown under various non-steady-state conditions. (A) Pulse energy 4.1 nJ, laser frequency 400 Hz, scanning rate 400 nm/s. (B) Pulse energy 4.8 nJ, laser frequency 400 Hz, scanning rate 1 μm/s. (C) Pulse energy 4.1 nJ, laser frequency 1000 Hz, scanning rate 1 μm/s.

Based on the physical principles of laser-induced liquid-phase epitaxy, this morphological transition can be interpreted through two primary mechanisms.

First, the phenomenon arises from the mismatch between the scanning speed and the intrinsic horizontal growth rate of the silicon. A stable growth morphology relies on the dynamic matching between the translation of the laser spot and the epitaxial deposition rate. When the scanning speed significantly exceeds the horizontal growth rate, the growth front can no longer "track" the center of the moving laser spot. Consequently, a spatial lag occurs where the majority of the laser energy is directed at the substrate ahead of the growth direction, leaving the pillar top at the cooler periphery of the thermal field. This lag leads to a drastic reduction in local heat input, causing the heat affected zone (HAZ) at the top to contract significantly. Since the epitaxial process is thermally driven, the shrunken HAZ restricts the radial dimensions of the nanostructure, inducing the evolution toward a sharper "tip" morphology.

Second, the high scanning speed triggers morphological instability at the growth surface. During rapid movement, minor fluctuations in the concentration field of precursor decomposition and the temperature gradient - potentially amplified by disturbances in the liquid-phase flow - lead to localized instabilities at the solid-liquid interface. Before the vertical growth interruption, these instabilities manifest as the observed micro-protrusions (small particles) at the pillar tip.

Regarding the crystallinity of these features, we have made systematic attempts at characterization. However, due to the extremely small size of these particles (typically < 30 nm) and their random distribution, nanoscale site-specific slicing using a FIB presents immense technical challenges. Positioning deviations during the preparation process make it exceptionally difficult to accurately capture these sub-30 nm particles within a TEM lamella. Nevertheless, while direct TEM

cross-sectional data for these specific tip particles are currently unavailable, a reliable inference can be drawn from similar features observed on the surfaces of horizontal silicon wires (Fig. S15). Characterization of those protrusions confirms a coherent epitaxial structure identical to the main body of the wire. Given the similar growth mechanism -the same precursor and thermally induced -it is highly probable that the tip region and its associated micro-protrusions maintain their single-crystal epitaxial nature.

In summary, the "tip" feature and micro-protrusions are products of the laser scanning speed approaching or exceeding the horizontal growth rate limit of vertical silicon pillars, representing morphological instability in high-dynamic processes. While the exact formation dynamics remain a subject for further investigation, these observations do not compromise the core conclusion regarding the controllable growth of single-crystal silicon nanostructures.

9. Horizontal silicon wires of different sizes.

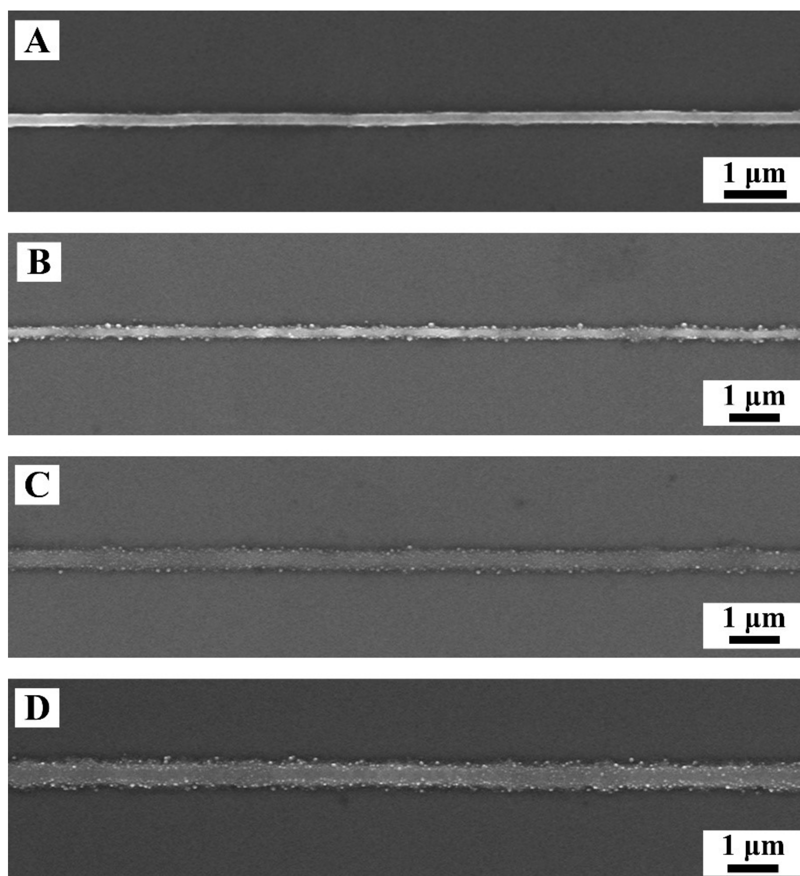

Fig. S8 SEM characterization of horizontal silicon nanowires with tunable dimensions. This figure presents SEM images of horizontal silicon nanowires grown at a constant laser frequency of 400 Hz under varying experimental conditions. (A) The nanowire grown with a single-pulse energy of 4.1 nJ and a scanning speed of 1 μm/s over 1 repeated scan. The resulting structure exhibits a full width at half maximum (FWHM) of 170±6 nm and a height of 185±7 nm. (B) The nanowire grown with a single-pulse energy of 4.8 nJ and a scanning speed of 11 μm/s over 5 repeated scans. The resulting structure exhibits a full width at half maximum (FWHM) of 200±8 nm and a height of 120±9 nm. (C) The nanowire grown with a pulse energy of 5.8 nJ and a scanning speed of 12 μm/s with 5 repeated scans, which yields a wider FWHM of 310±13 nm and a height of 115±8 nm. (D) The nanowire grown with a pulse energy of 6.7 nJ and a scanning speed of 13 μm/s with 7 repeated scans. This configuration results in an FWHM of 420±14 nm and a height of 176±9 nm.

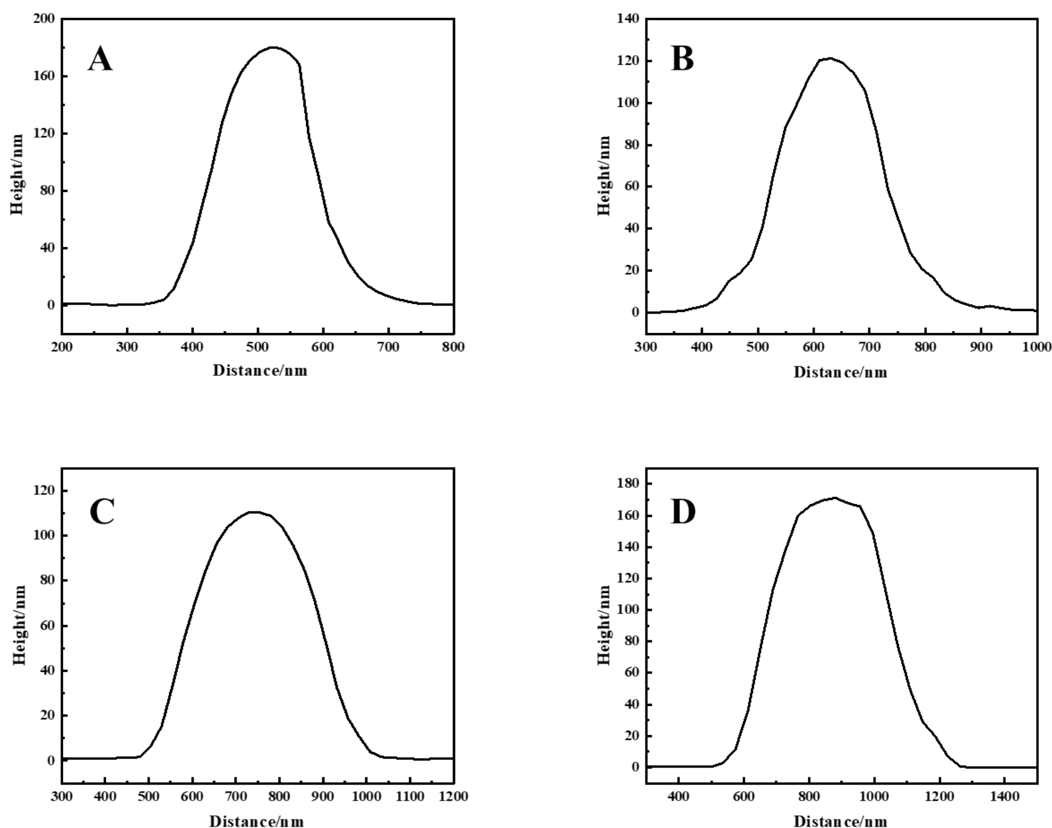

Fig. S9 AFM height profiles of Si nanowires grown under varied experimental conditions. (A) Pulse energy of 4.1 nJ, scanning speed of 1 μm/s, and 1 scan; (B) 4.8 nJ, 11 μm/s, and 5 repeated scans; (C) 5.8 nJ, 12 μm/s, and 5 repeated scans; (D) 6.7 nJ, 13 μm/s, and 7 repeated scans.

To confirm the crystallinity, we performed TEM characterizations on horizontal nanowires grown under various conditions along the transverse and oblique cross-section. TEM results (Fig. S10-12) showed that, in all cases, the SAED patterns remained perfectly coherent with the Si substrate. The atomic arrangement shows no discernible dislocations or grain boundaries. These results definitively confirm that the horizontal nanowires are homoepitaxially grown single crystals.

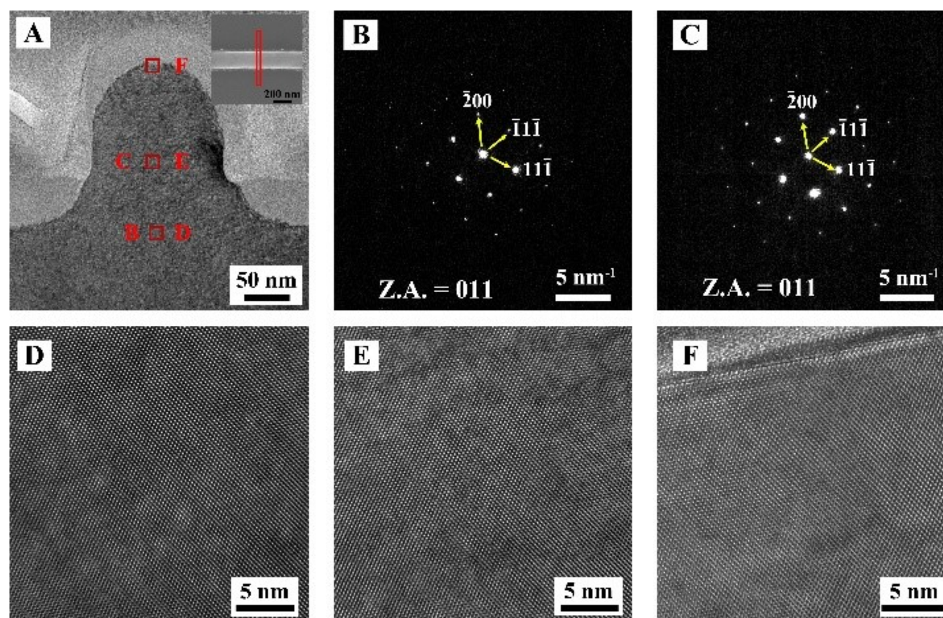

Fig. S10 Cross-sectional TEM characterization of a horizontal Si nanowire grown with a pulse energy of 4.1 nJ, a repetition rate of 400 Hz, and a scanning speed of 1 μm/s with 1scan. (A) Bright-field TEM image of the transverse cross-section. (B, C) SAED patterns obtained from the boxed regions indicated in (A). (D-F) HRTEM images of the boxed regions in (A) captured along the [011] zone axis (Z.A.).

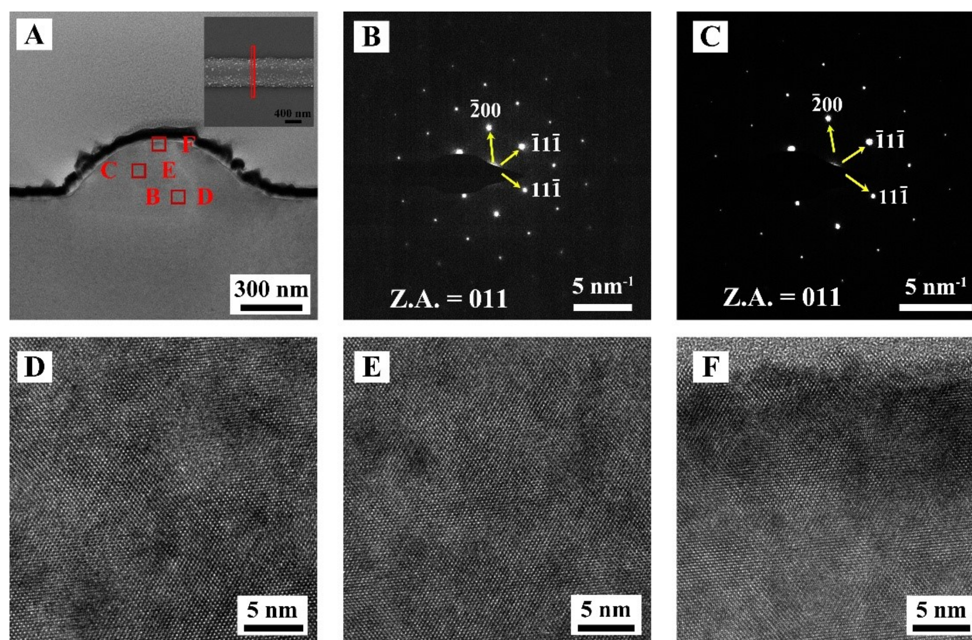

Fig. S11 Cross-sectional TEM characterization of multi-scan horizontal silicon nanowire. The structural and crystallographic properties of a nanowire grown at 6.7 nJ, 400 Hz, 13 μm/s and 7 repeated scans was examined. (A) Bright-field TEM cross-sectional image of the nanowire. (B, C) SAED patterns obtained from the boxed region shown in A. (D-F) HRTEM images viewed along the [011] Z.A. from the boxed region shown in A.

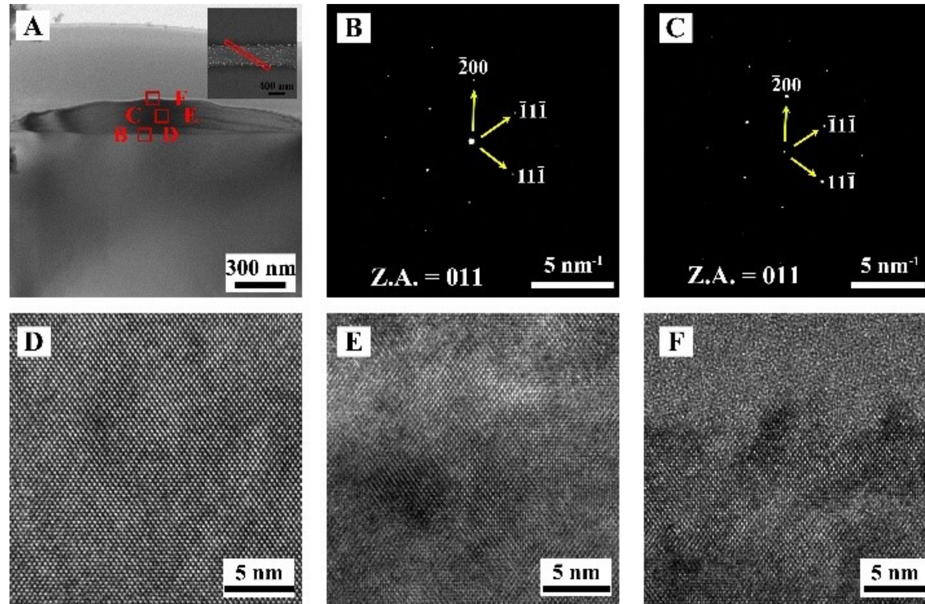

Fig. S12 Oblique cross-sectional TEM characterization of a heavily doped horizontal Si nanowire synthesized with a pulse energy of 6.7 nJ, a repetition rate of 400 Hz, and a scanning speed of 13 μm/s with 7 repeated scans. (A) Bright-field TEM image of the oblique cross-section. (B, C) SAED patterns obtained from the boxed regions indicated in (A). (D-F) HRTEM images of the boxed regions in (A) captured along the [011] zone axis (Z.A.).

Regarding the growth mechanism of the horizontal Si nanowires, analysis based on multiphysics simulations and liquid-phase epitaxial growth processes indicates that the transition from vertical to horizontal growth is driven by the synergy of thermal field deflection and geometry-dependent kinetics (Fig. S13). At high scanning speeds (1 μm/s), a pronounced spatial lag emerges between the growth front and the center of the laser energy distribution. For a simulation model featuring a silicon hemisphere with a radius of 85 nm - a dimension rationalized by the experimentally observed full width at half maximum (FWHM) of 170 nm for horizontal nanowires - and a vertical growth rate of 500 nm/s, the calculated offset distance expands from approximately 60 nm (characteristic of vertical pillar growth) to 170 nm for the horizontal nanowire regime. This shift causes the heat affected zone (HAZ) to migrate from the apex to the flanks of the nanostructure and onto the forward substrate (Fig. S13A), thereby guiding silicon deposition along the horizontal scanning trajectory. Furthermore, according to the Gibbs-Thomson relation, the energy barrier for nucleation and epitaxial growth is significantly lower at concave surfaces due to reduced surface energy requirements. The junction between the growing nanostructure and the substrate thus forms a natural concave site (Fig. S13B), which serves as a preferential growth front and facilitates continuous horizontal expansion. Consequently, the combination of this thermal field bias and the preferential kinetics at the concave growth interface enables the reliable synthesis of continuous horizontal nanowires.

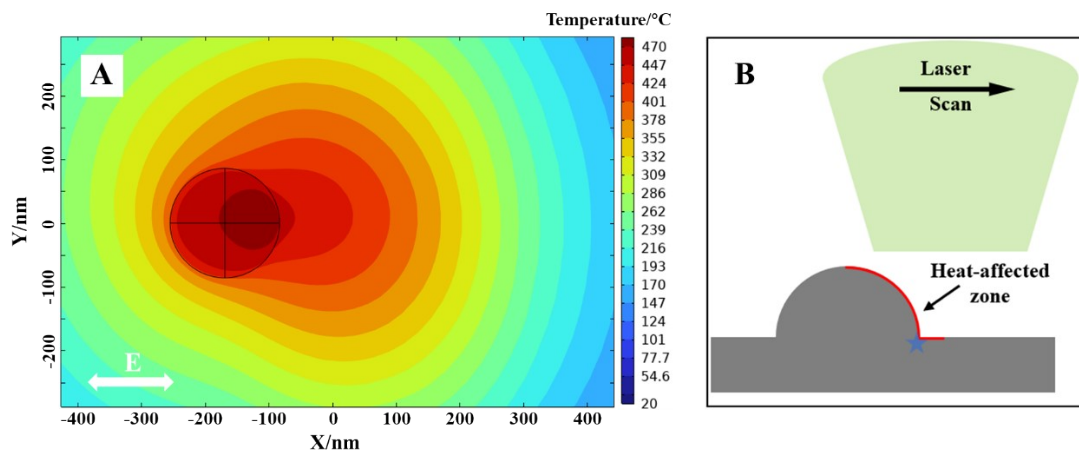

Fig. S13 Horizontal silicon wire continuous epitaxial growth mechanism based on thermal field deflection. (A) Thermal field distribution on the growth surface under laser scanning irradiation; (B) Schematic diagram of thermal field deflection on the growth surface.

The following section provides a detailed clarification regarding the scanning trajectory of the horizontal Si nanowires and the nature of the bright spots observed on their surfaces (Fig S7B-D).

Firstly, the scanning path description for horizontal nanowires refers to the linear trajectory of the laser focus relative to the substrate. During laser scanning irradiation process, the substrate moves at a constant velocity in the horizontal plane while the laser remains active. For "repeated scans," the laser focus re-traces the exact same linear trajectory for a specified number of cycles. In our results, the path taken by the laser corresponds precisely to the longitudinal axis of the grown nanowires.

Secondly, regarding the bright dots in Fig. S8B-D, we have conducted additional high-magnification SEM characterizations (Fig. S14). These "dots" are confirmed to be minor silicon protrusions on the nanowire surface. HRTEM and its fast Fourier transform (FFT) analysis (Fig. S15) demonstrate that these protrusions are not foreign impurities. Instead, they exhibit homoepitaxial growth with perfect lattice continuity relative to the main nanowire body. No heterostructures or grain boundaries were detected at the interface between the protrusions and the nanowire. The high brightness in SEM images is attributed to the edge effect in SE mode. Due to the high local curvature of these small protrusions, the secondary electron yield is significantly enhanced, manifesting as bright spots.

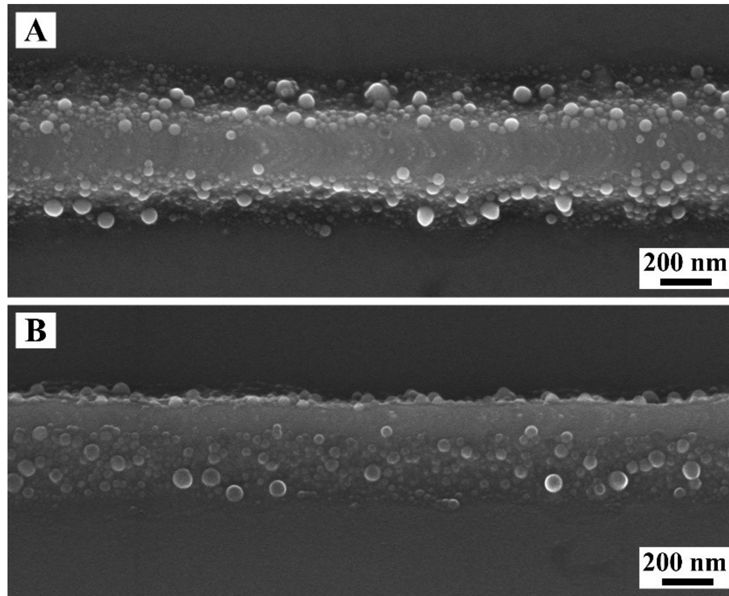

Fig. S14 High-resolution SEM images of a horizontal Si nanowire grown using a pulse energy of 6.7 nJ, a repetition rate of 400 Hz, and a scanning speed of 13 μm/s with 7 repeated scans. (A) Top-down view; (B) 45° tilted view.

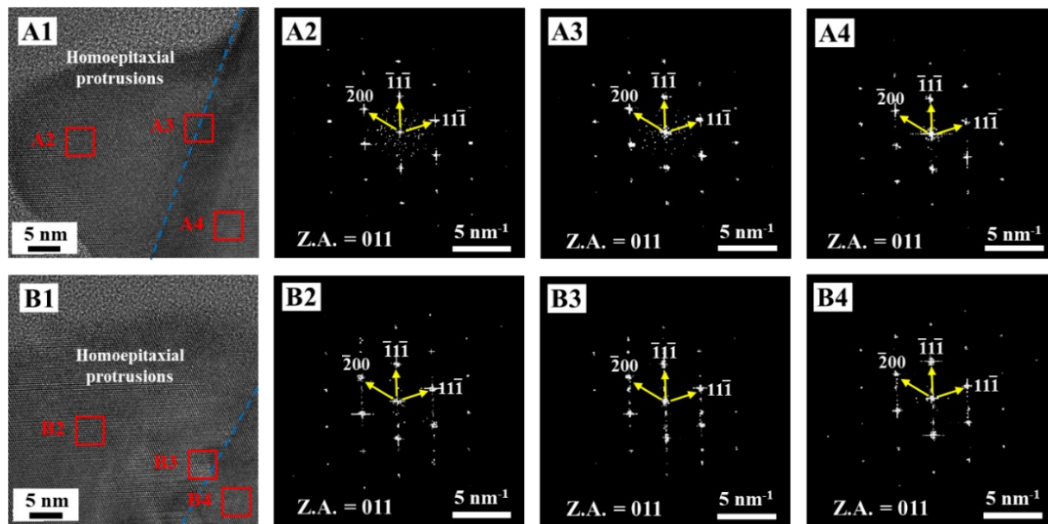

Fig. S15 HRTEM images and corresponding FFT analysis of the surface protrusions on Si nanowires. (A1, B1) HRTEM images of the protrusions, where the blue dashed lines delineate the interface between the protrusion and the main nanowire body. (A2-A4) and (B2-B4) present the FFT patterns obtained from the regions indicated by the red squares in (A1) and (B1), respectively.

While a definitive mechanism is still under investigation, we hypothesize that these protrusions originate from localized interfacial instabilities. During laser-induced liquid-phase epitaxy, transient fluctuations in the local thermal field or the decomposition rate of the precursor on the growth surface can occur. At high scanning speeds, such perturbations may cause the liquid-solid growth interface to become momentarily unstable, leading to the formation of random, small-scale epitaxial outgrowths.

Although these features indicate that growth control at smaller scales could be further refined,

we emphasize that the current results represent the product of systematically optimized parameters (pulse energy, frequency, scan speed, etc.). Crucially, since these protrusions maintain the same crystal structure and orientation as the main nanowire, they do not compromise the single-crystalline integrity of our results or the validity of our proposed growth mechanism.

10. Formation Mechanisms and Parameter-Dependent Modulation of Elliptical Cross-sections in Silicon Pillars

Firstly, regarding the physical origins of the elliptical cross-sections in the Si nanopillars is related to the photothermal field distribution and the underlying growth kinetics.

1. As described in the fourth paragraph of Section 3.2, the simulated photothermal field in Fig. 3A is indeed an ellipse elongated along the X-axis (polarization direction), rather than a perfect circle. This is most evident in the innermost deep-red isothermal contours. Since the epitaxial growth is initiated by the localized thermal decomposition of CHS, the contour of this heat-affected zone directly dictates the effective physical boundaries for atom deposition. Consequently, the elliptical thermal distribution inherently leads to a higher deposition probability and extended growth range along the polarization axis.

2. FDTD simulations show that as the silicon nanostructure nucleates and grows, its interaction with the incident laser triggers a Mie resonance effect. This redistributes the localized electric field from a circular Gaussian profile into a double-lobe distribution elongated along the polarization direction (X-axis, Fig. S16A, B). While the CHS precursor does not directly absorb 532 nm light, its thermal decomposition produces various polar silicon radical intermediates with significant dipole moments. The enhanced local electric field exerts a directional induction force on these dipoles, guiding them to accumulate in regions of high field intensity. This localized concentration enrichment and alignment increase the effective collision probability of reactive species on the growth surface (Fig. S16C), effectively lowering the reaction barrier and accelerating the deposition kinetics along the polarization axis.

The synergy between the elliptical thermal field and this field-driven kinetic acceleration results in the observed elliptical cross-sections of the silicon pillars.

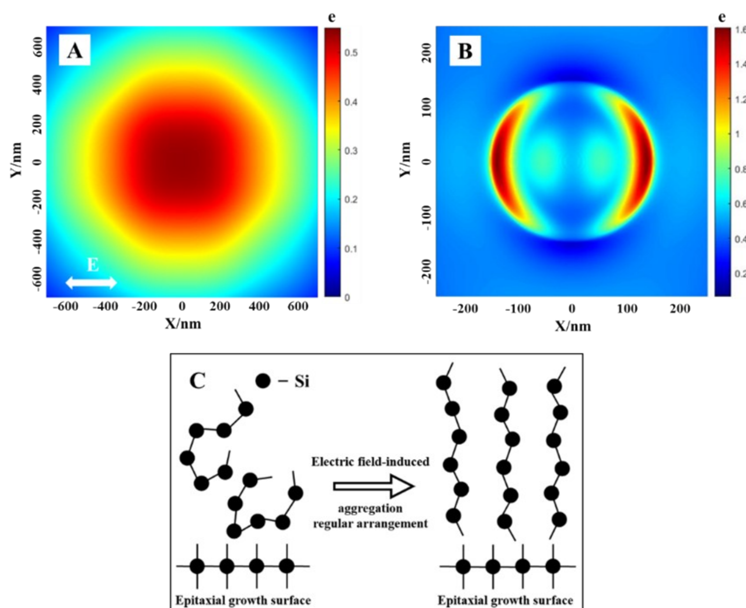

Fig. S16 Polarization-induced deformation of electric field distribution and its influence on localized epitaxial growth kinetics. (A) Simulated electric field intensity distribution on a planar substrate under laser irradiation; *e* denotes the relative enhancement factor. (B) Electric field intensity distribution on a substrate featuring a silicon hemisphere with a radius of 85 nm. (C) Schematic illustration of the epitaxial growth kinetics modulated by the localized electric field.

Secondly, regarding the evolution of the cross-sectional morphology, four key parameters were systematically investigated. To clarify the experimental conditions, scanning speed was studied under the scanning irradiation mode, while laser pulse energy, irradiation time, and laser frequency were investigated under the stationary (steady-state) irradiation mode. The results are summarized as follows:

Regarding the scan rate, when the scanning speed increases from 50 nm/s to 100 nm/s (at 4.1 nJ, 400 Hz), no significant change was observed at the pillar top (Fig. S17). The long and short axes were 340±13 nm and 240±11 nm, respectively. At a higher speed of 200 nm/s, where the tilt angle significantly increases, the cross-section appears further elongated and flattened along the polarization direction in SEM images, although precise measurement becomes more challenging.

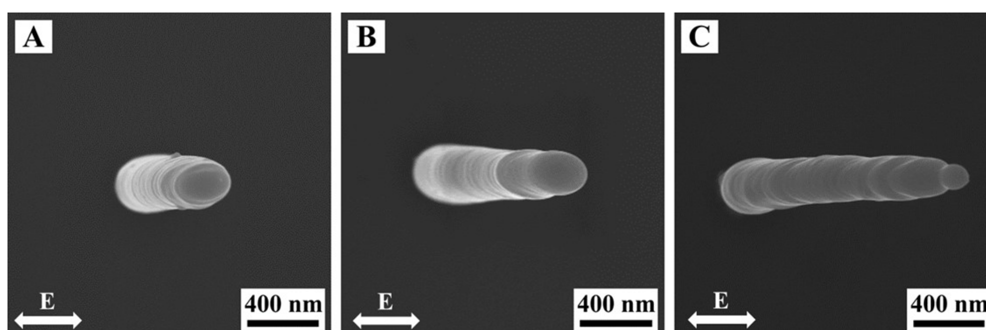

Fig. S17 SEM images of curved silicon pillars grown at various scanning speeds with a pulse energy of 4.1 nJ and a laser frequency of 400 Hz. (A) 50 nm/s; (B) 100 nm/s; (C) 200 nm/s

Regarding the laser pulse energy, as the single-pulse energy increases from 4.1 nJ to 5.1 nJ (at 400 Hz, 7 s), both the short and long axes increase proportionally (short axis: 310±10 nm to 400±17 nm; long axis: 450±13 nm to 580±16 nm. Fig. S18).

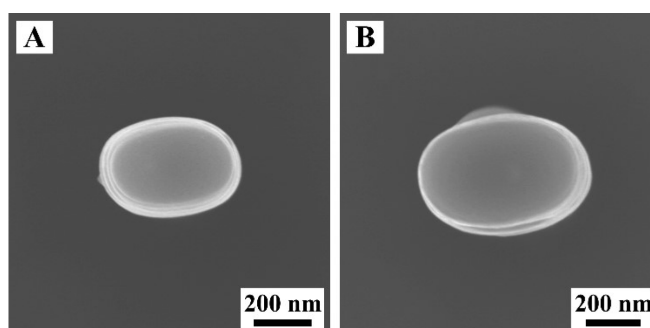

Fig. S18 SEM images of vertical silicon pillars grown at various pulse energies with a laser frequency of 400 Hz and a static irradiation time of 7 s. (A) 4.1 nJ; (B) 5.1 nJ.

Regarding the irradiation time, extending the irradiation time (at 4.1 nJ, 400 Hz) does not noticeably alter the cross-sectional dimensions, with the axes remaining stable at 450±13 nm and 310±10 nm (Fig.S19).

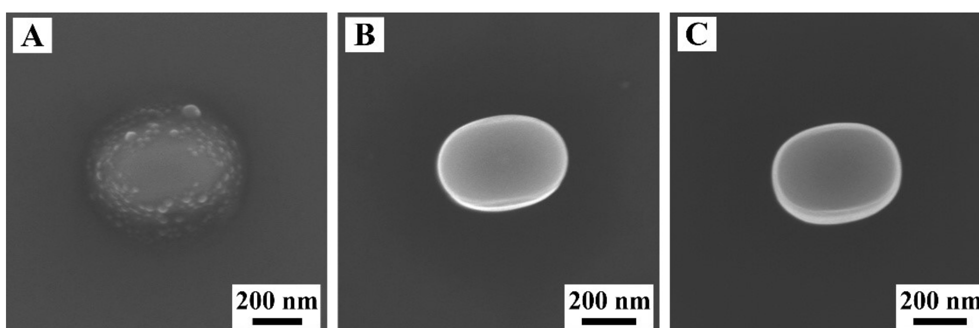

Fig. S19 SEM images of vertical silicon pillars grown at various irradiation times with a pulse energy of 4.1 nJ and a laser frequency of 400 Hz. (A) 1 s; (B) 3 s; (C) 5 s.

Regarding the laser frequency, while the short axis remains constant at 310±10 nm as the frequency increases from 400 Hz to 2000 Hz (at 4.1 nJ), the long axis exhibits a shortening trend from 450±13 nm to 415±14 nm (Fig.S20). This suggests that frequency-dependent growth kinetics specifically influence the growth along the polarization axis.

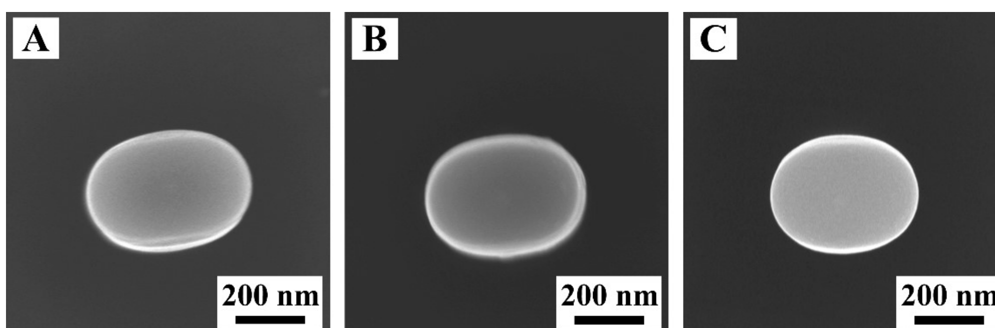

Fig. S20 SEM images of vertical silicon pillars grown at various laser frequencies and irradiation times with a pulse energy of 4.1 nJ. (A) 400 Hz, 5 s; (B) 1000 Hz, 1 s; (C) 2000 Hz, 0.5 s.

These results indicate that the minor axis of the elliptical cross-section is primarily dictated by the single-pulse laser energy. The underlying mechanism is rooted in the thermal dynamics characterized in our previous study.[1] By employing a nanosecond pulsed laser with a short pulse width (6 ns) and low repetition rate (400 Hz), the thermal accumulation between successive pulses is rendered negligible. Each nanosecond pulse induces a transient heating event followed by a rapid return to ambient temperature; consequently, the epitaxial growth of silicon occurs as a discontinuous process that initiates with the pulse onset and terminates upon its conclusion. Therefore, among the parameters of pulse energy, frequency, and irradiation time, only variations in the single-pulse energy modulate the spatial extent of the high-temperature zone on the substrate, thereby governing the lateral dimensions of the nanopillars. In contrast, the laser frequency and irradiation time predominantly influence the growth rate and the final height of the structures.

In contrast, the major axis of the elliptical cross-section is influenced not only by the single-pulse energy but also by the pulse frequency. This suggest that the evolution of the major axis is not solely dictated by the static photothermal distribution; rather, it is also likely governed by the interplay between mass transport and growth kinetics. The peak temperature localized at the focal center induces the most rapid consumption of precursor species in this region. At higher frequencies (faster growth rates), a localized depletion zone is established at the center of the laser spot. This

depletion region impedes mass transport along the polarization axis - the zone of enhanced electric field - thereby restricting the diffusion-mediated supply of reactive precursors toward the peripheral growth front. The competition between rapid consumption and restricted diffusion leads to the observed shortening of the major axis. While this inference is grounded in the fundamental physical principles of epitaxial growth and mass transport, we acknowledge that further systematic investigations are required to establish a definitive conclusion.

11. Elemental quantification of phosphorus-doped silicon nanowires.

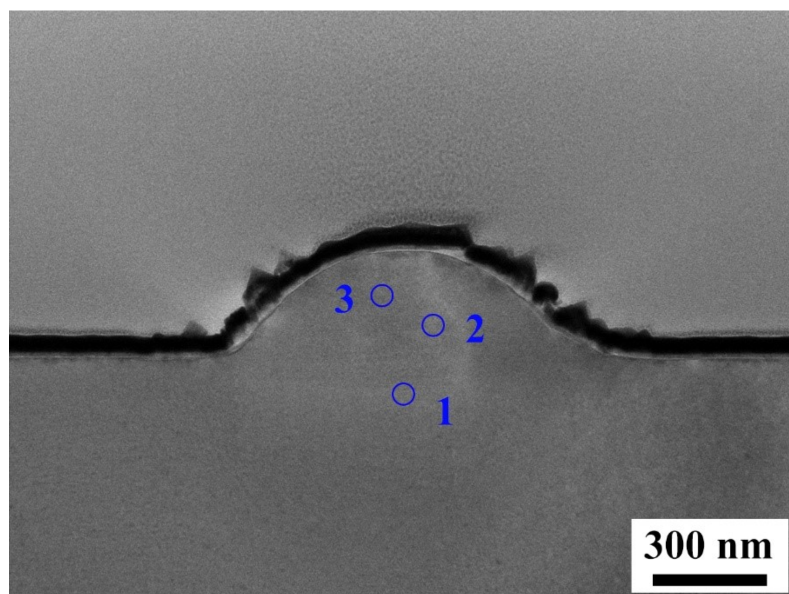

Fig. S21 A bright-field TEM image displays the cross-section of a silicon nanowire grown under high-energy conditions (6.7 nJ, 13 μm/s, 7 repeated scans). The blue circles denote the specific regions where energy-dispersive X-ray spectroscopy (EDS) was performed.

To confirm the spatial distribution and concentration of phosphorus dopants, Energy-Dispersive X-ray Spectroscopy (EDS) point analysis was conducted at three distinct locations (indicated by blue circles in Fig. S21). The results, summarized in Table S2, demonstrate compositional uniformity throughout the nanowire volume, with an average phosphorus atomic fraction of 2.53%. In contrast, no phosphorus signal was detected within the high-resistance silicon substrate.

Table S2. EDS point analysis results at different locations

Position	Element	Atomic fraction
1	Si	100%
	P	0
2	Si	97.40%
	P	2.60%
3	Si	97.54%
	P	2.46%

12. SEM images of heavily doped silicon nanowires and electrodes.

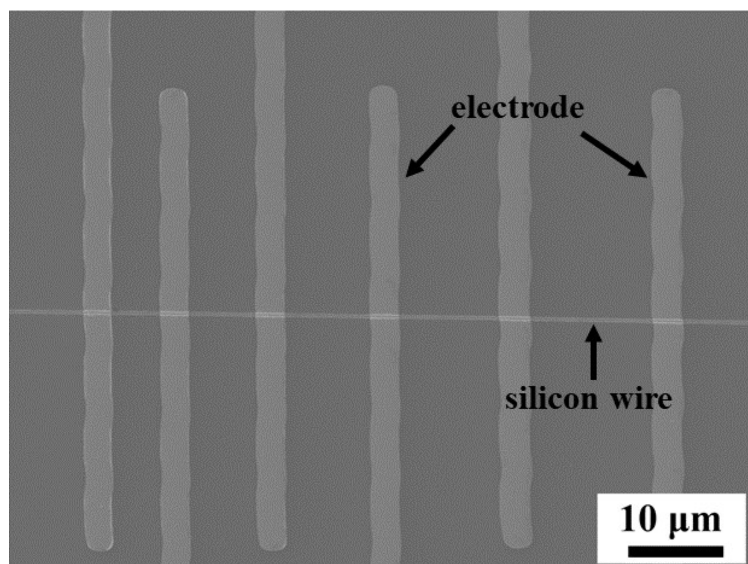

Fig. S22 SEM characterization of a heavily doped horizontal silicon nanowire and its integrated electrode configuration. This image was captured from a top-down perspective to illustrate the spatial arrangement of the nanowire and the contact pads. The electrodes were fabricated as a three-layer metallic architecture comprising titanium (Ti), aluminum (Al), and platinum (Pt) to ensure reliable electrical connectivity for transport measurements.[11]

13. Cross-sectional area of phosphorus-doped silicon nanowires and its effect on electrical properties

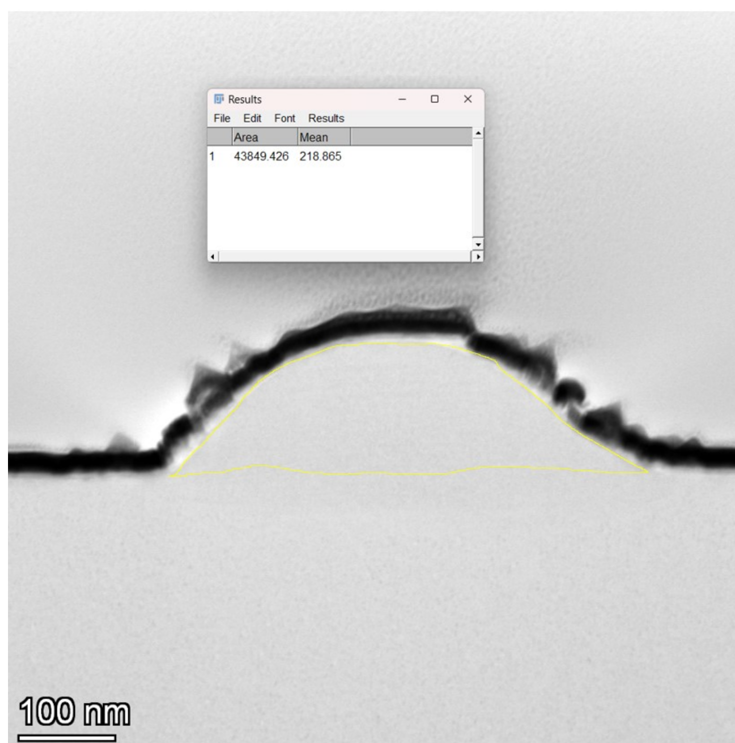

Fig. S23 Quantitative cross-sectional area analysis of multi-pass silicon nanowire. The image illustrates the boundary-fitting analysis performed on a nanowire cross-section (6.7 nJ, 13 μm/s, 7 passes) using ImageJ software. The effective cross-sectional area was calculated to be approximately 4.4×10^{-2} μm^2.

The potential influence of cross-sectional morphological non-uniformity on the extracted electrical parameters of the Si nanowires was assessed within the framework of the transmission line model (TLM). The resistivity measurement principle utilized in this study is based on fabricating a series of metal electrodes with varying gap distances (L) on a single horizontal Si nanowire to measure the total resistance (R_{total}) between adjacent electrodes. According to TLM, R_{total} is the linear superposition of the nanowire's volumetric resistance ($R_v = (\rho/A)\cdot L$) and the contact resistance (R_c), expressed as $R_{total} = (\rho/A)\cdot L + 2R_c$, where ρ is the resistivity and A is the cross-sectional area. By performing a linear regression on the R_{total}-L experimental data, the slope $k = \rho/A$ is obtained. The resistivity is then calculated as $\rho = k\cdot A$, using the cross-sectional area determined from FIB-slicing characterization.

From a fundamental measurement perspective, the resistance recorded for each segment represents the cumulative effect of localized resistivity over the electrode spacing (L). Consequently, this process inherently provides a statistically averaged resistivity, which effectively mitigates the impact of random localized fluctuations in the cross-sectional area (A). Furthermore, SEM images of the horizontal Si nanowires (Fig. S24A) demonstrate high width uniformity along the growth direction. To quantitatively assess this morphological consistency, AFM characterization was conducted on a representative 3 μm segment (Fig. S24B). Five independent measurements at different positions (Table S3) yielded an average FWHM of 417±24 nm and a height of 176±5 nm.

The resulting relative standard deviations (RSD) are approximately 5.8% for width and 2.8% for height, further confirming the size consistency of the grown nanowire.

Based on the analysis above, it can be concluded that the conductivity errors induced by minor geometric deformations fall within an acceptable range and do not alter the fundamental conclusions regarding the heavy doping characteristics and electrical performance discussed in this study.

It should be clarified that the mean values and standard deviations presented here refer to the statistical results at different positions along a single Si nanowire (intra-wire variation). In contrast, the statistics discussed in other sections describe the average dimensions of different nanowires obtained from multiple independent experiments (inter-wire repeatability). Given the distinct statistical targets, their respective results naturally differ.

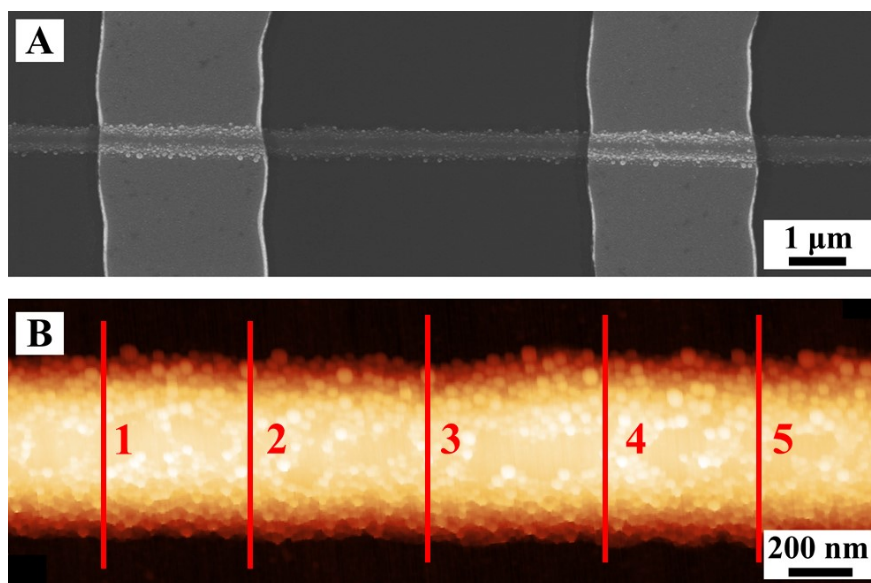

Fig. S24 Morphological characterization of heavily doped horizontal Si nanowires. (A) SEM image of a horizontal Si nanowire integrated with metal electrodes, synthesized using a pulse energy of 6.7 nJ, a repetition rate of 400 Hz, and a scanning speed of 13 μm/s with 7 repeated scans; (B) AFM topographic scan of the horizontal Si nanowire.

Table S3. FWHM and height of a Si nanowire measured by AFM at various positions.

Position	Full width at half maximum (FWHM, nm)	Height (nm)
1	418	180
2	397	182
3	388	172
4	448	177
5	433	170
Average value	416.8	176.2
Relative standard deviations (RSD)	24.8	5.1

References

1. X. Yang, P. Chen and Z. Liu, *Additive Manufacturing*, 2025, **114**, 105029.
2. B. A. Joyce, R. R. Bradley and G. R. Booker, *The Philosophical Magazine: A Journal of Theoretical Experimental and Applied Physics*, 1967, **15**, 1167-1187.
3. T. Shimoda and T. Masuda, *Japanese Journal of Applied Physics*, 2014, **53**, 02BA01.
4. E. D. Palik, *Handbook of Optical Constants of Solids*, Academic Press, 1998.
5. A. J. Sabbah and D. M. Riffe, *Physical Review B*, 2002, **66**, 165217.
6. M. Hase, M. Kitajima, A. M. Constantinescu and H. Petek, *Nature*, 2003, **426**, 51-54.
7. T. Sjodin, H. Petek and H.-L. Dai, *Physical Review Letters*, 1998, **81**, 5664-5667.
8. Y. Liao, S. Zhang, Z. Tang, X. Liu and K. Huang, *RSC Advances*, 2017, **7**, 26546-26550.
9. K.-m. Huang and Y.-h. Liao, *IEEE Transactions on Microwave Theory and Techniques*, 2015, **63**, 135-140.
10. G. E. Jellison and F. A. Modine, *Journal of Applied Physics*, 1994, **76**, 3758-3761.
11. A. Motayed, J. E. Bonevich, S. Krylyuk, A. V. Davydov, G. Aluri and M. V. Rao, *Nanotechnology*, 2011, **22**, 075206.